

Supplementary information for “Imaging the Lithospheric Structure beneath the Indian continent”

S. Maurya¹, J.-P. Montagner¹, M. Ravi Kumar², E. Stutzmann¹, S. Kiselev³, G. Burgos¹, N. Purnachandra Rao² and D. Srinagesh²

1: Institut de Physique du Globe de Paris, France (maurya@ipgp.fr)

2: National Geophysical Research Institute, Hyderabad, India

3: Institute of Physics of the Earth, Moscow, Russia

S1. Seismic station and azimuthal data coverages

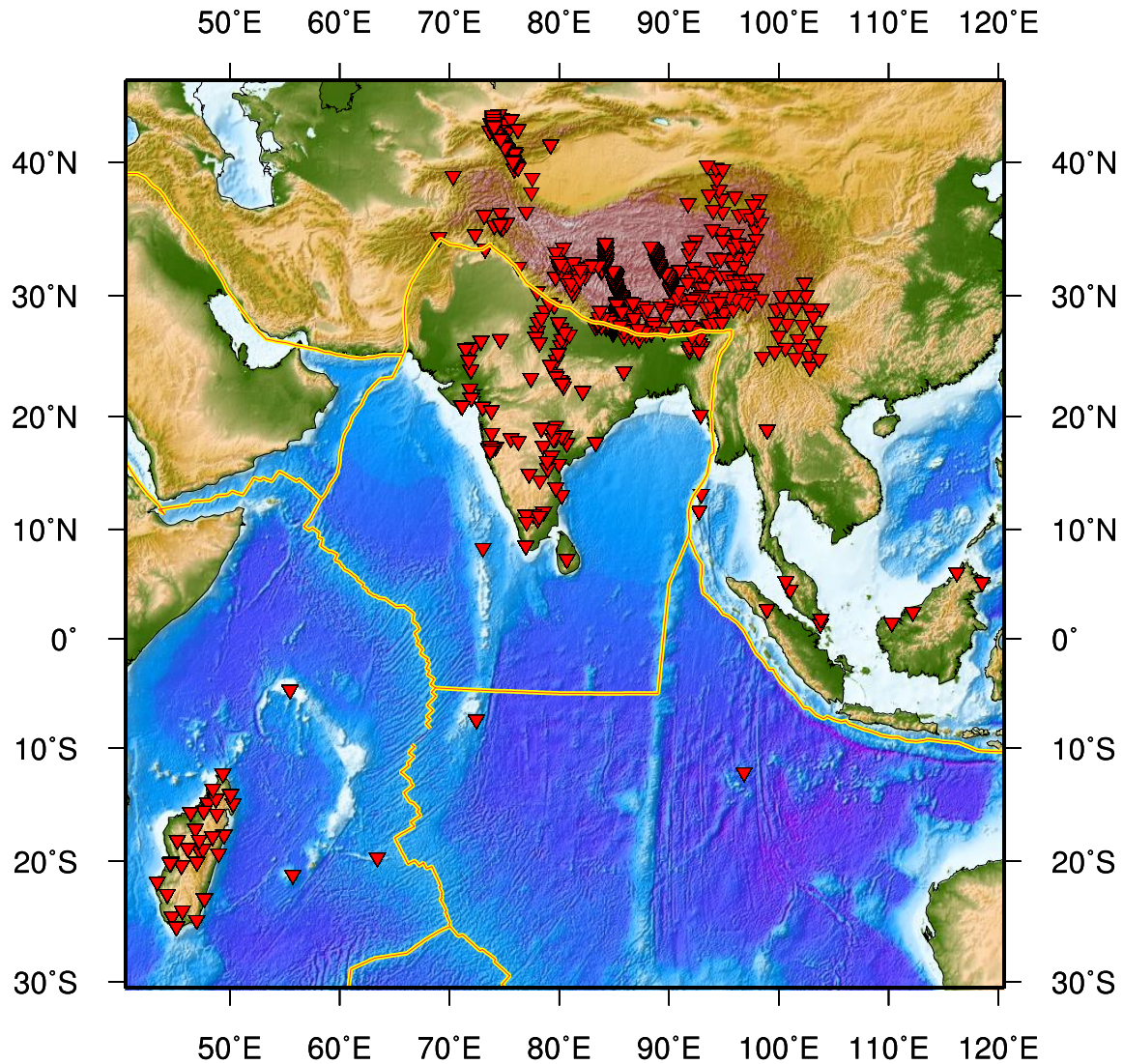


Figure S1.1: Geographical distribution of the seismic stations of the global and regional networks.

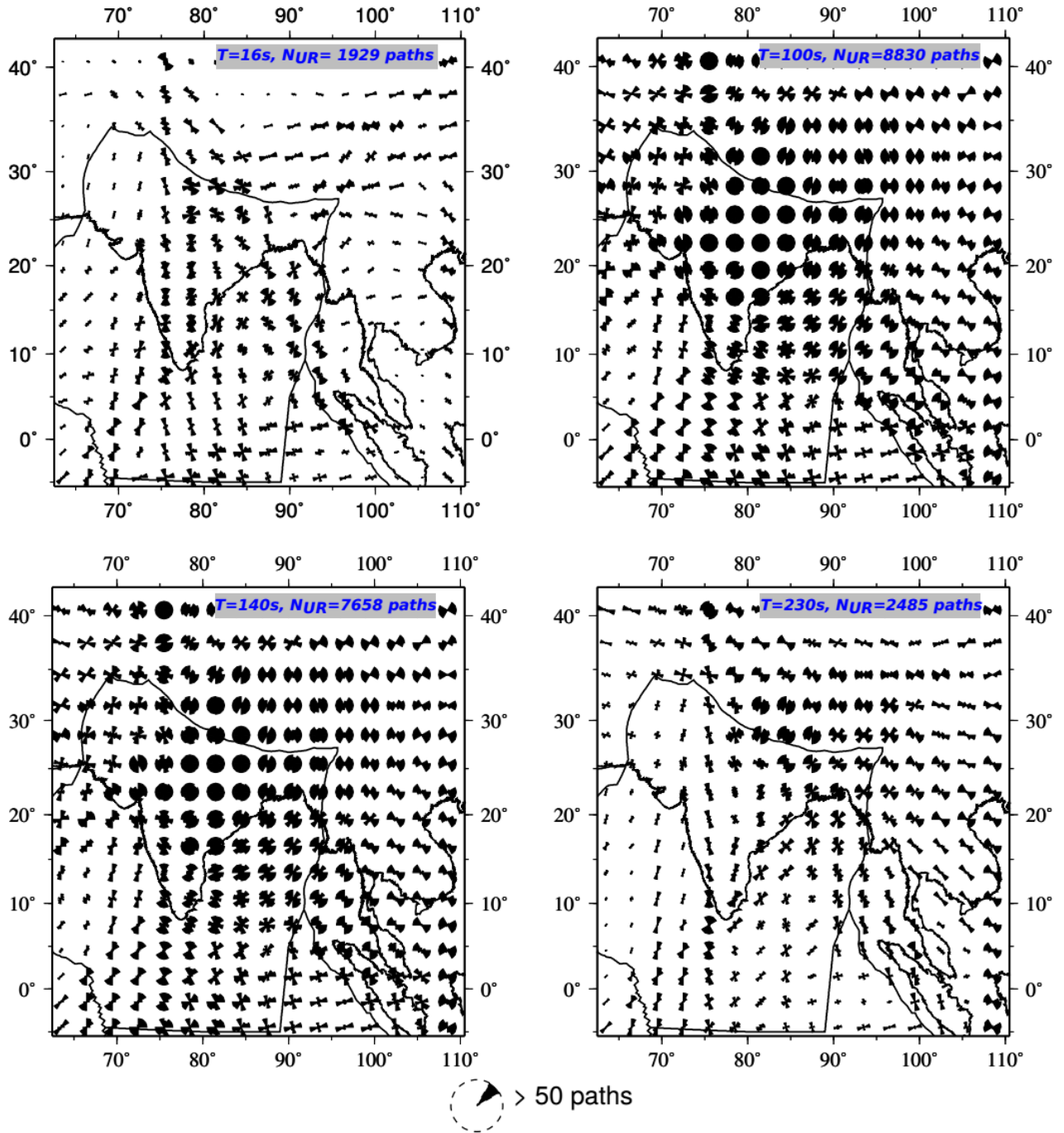


Figure S1.2: Azimuthal coverage of the data used for determination of Rayleigh wave group velocities at 16, 100, 140 and 230s with the respective number of paths N_{UR} (in top right). The number of paths per unit area ($3^\circ \times 3^\circ$ cell) are binned in the azimuth range of 30° . The vectors are saturated at 50 paths.

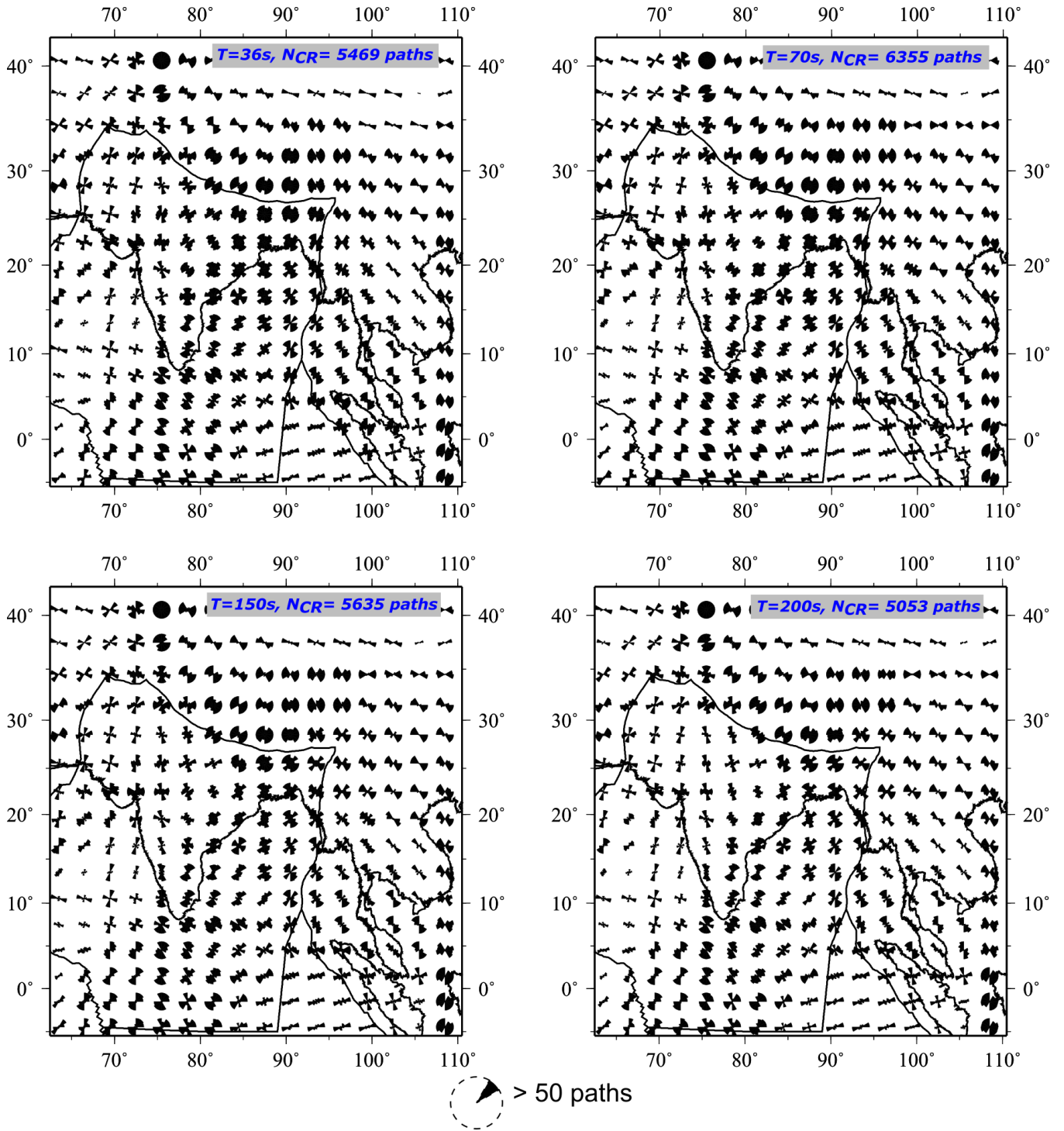


Figure S1.3: Azimuthal coverage of the data used for determination of Rayleigh wave group velocities at 36, 70, 150 and 200s with the respective number of paths N_{CR} (in top right). The number of paths per unit area ($3^\circ \times 3^\circ$ cell) are binned in the azimuth range of 30° . The vectors are saturated at 50 paths.

S2. Surface wave dispersion curves

S2.1. Example of group velocity dispersion

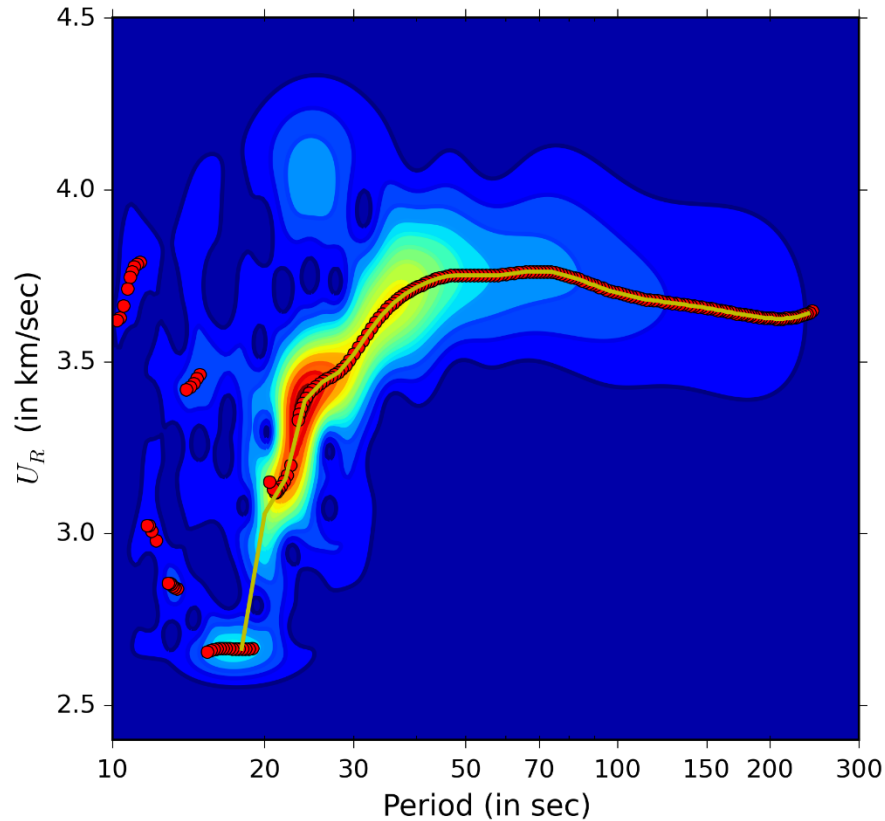


Figure S2.1: Rayleigh wave group dispersion curve corresponding to a seismogram shown in figure S2.3.4. The background color shows the FTA diagram. Red dots are the automatic picks on the FTA diagrams relative to maxima of the diagram. Red color denotes large amplitudes and the yellow curve is the manually picked dispersion curve avoiding outliers.

S.2.2 The Roller-coaster method:

- 1) Synthetic seismograms are modelled at the receiver using the normal mode summation method [Woodhouse and Girnius, 1982] for a given source and modified reference 1-D Earth model, PREM [Dziewonski and Anderson, 1981].
- 2) The seismogram is divided into two time windows corresponding to the higher modes (T_1 - T_2 , T_5 - T_6) and to the fundamental mode (T_3 - T_4 , T_7 - T_8) on the real and synthetic data

respectively as shown in figure S2.2.1, keeping the window same for both the waveforms. Only the T_3 - T_4 window is used for the fundamental mode.

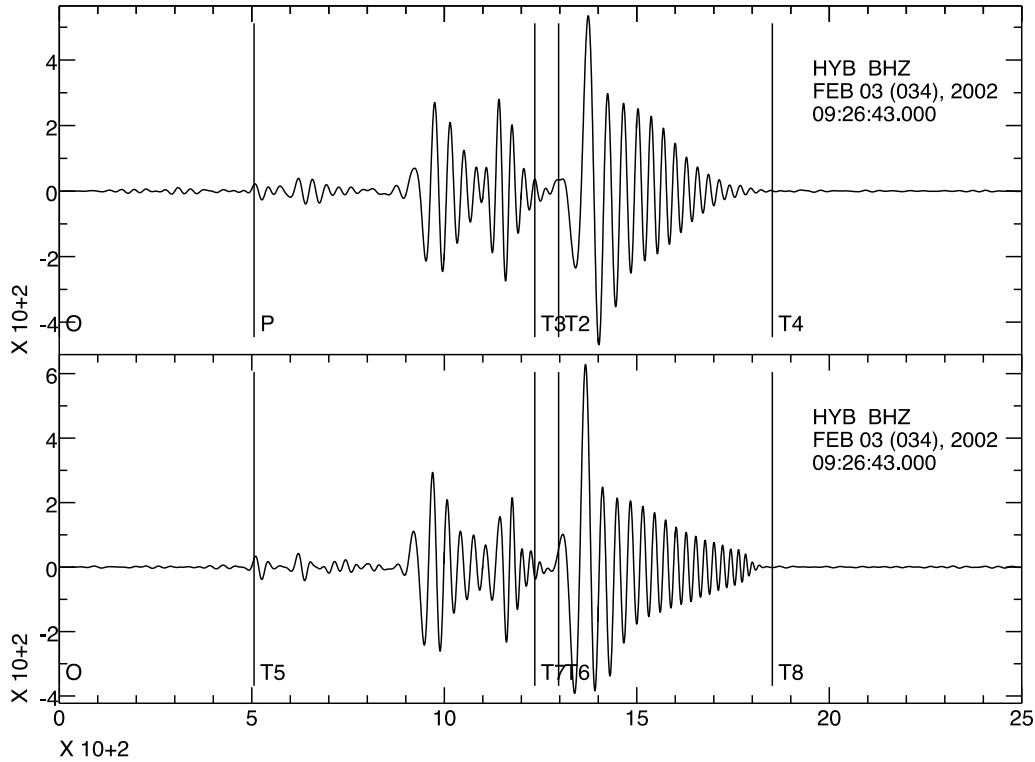


Figure S2.2.1: Above: Rayleigh waveforms computed from normal mode summation method. Data as synthetic seismogram (top) for small perturbations in the upper mantle PREM and starting reference synthetic seismogram (bottom) for reference starting model PREM.

3) The spectra of real and synthetic seismograms are computed and resampled with truncated windows (T_3 - T_4).

4) A gradient least-squares [Tarantola *et al.*, 1982] inversion scheme is adopted for modelling.

This compares the recorded and synthetic seismogram spectra and minimizes the misfit function between them. Initially, it explores all the large-scale variations over the model space and then the short-wavelength solution is found in the local variations of the misfit function.

5) The quality test of observed phase velocity is performed by the forward problem (eq. 1). A phase shift is applied to the synthetic data to accept or reject the observed measurements (fig. S2.2.2).

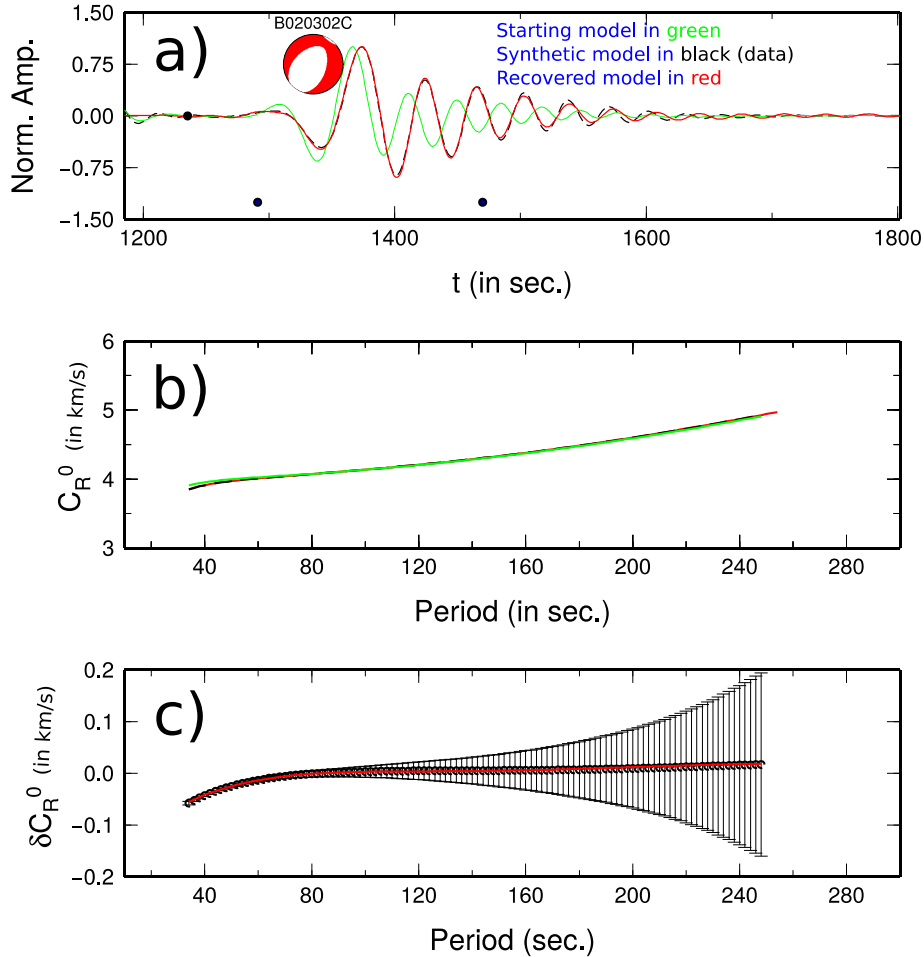


Figure S2.2.2: Plots showing the quality of our phase velocity measurements. The synthetic seismogram (data) computed by making small perturbations to the upper mantle PREM, recovered seismogram obtained using eq.1 after phase correction applied to the seismogram obtained by the starting model (PREM model) a) The recovered seismogram explains very well synthetic seismogram (data) b) phase velocity curves and c) phase velocity difference between the observed and recovered curves using the starting model. Two additional synthetic tests are presented in Figure S2.3.3 to show the effect of different starting models on the dispersion curve.

S2.3: Selection of starting model for phase velocity inversion:

The Roller coaster method is based on a gradient least-squares inversion algorithm and the inversion problem has a few challenges with regard to the starting model. When the starting

model is too far from the real one, the inversion methods may propagate large errors from long to short periods while exploring the solution. To minimize this issue and the nonlinear effects due to crust, we need to use a good starting model that explores better solutions. The average crustal structure is generally defined by two parameters: Poisson's ratio and crustal thickness. For regional and teleseismic events, the ray-paths across various complex structures between ocean-continent may possibly have very large variations due to the large lateral variation in crustal structure. In our study area, most of the seismic waves travel across large lateral heterogeneities in the crust around the Indian shield such as the thick crust in the Himalayas and Tibet (40-75km), thick sediments in the Bay of Bengal and the Indo-Gangetic plain.

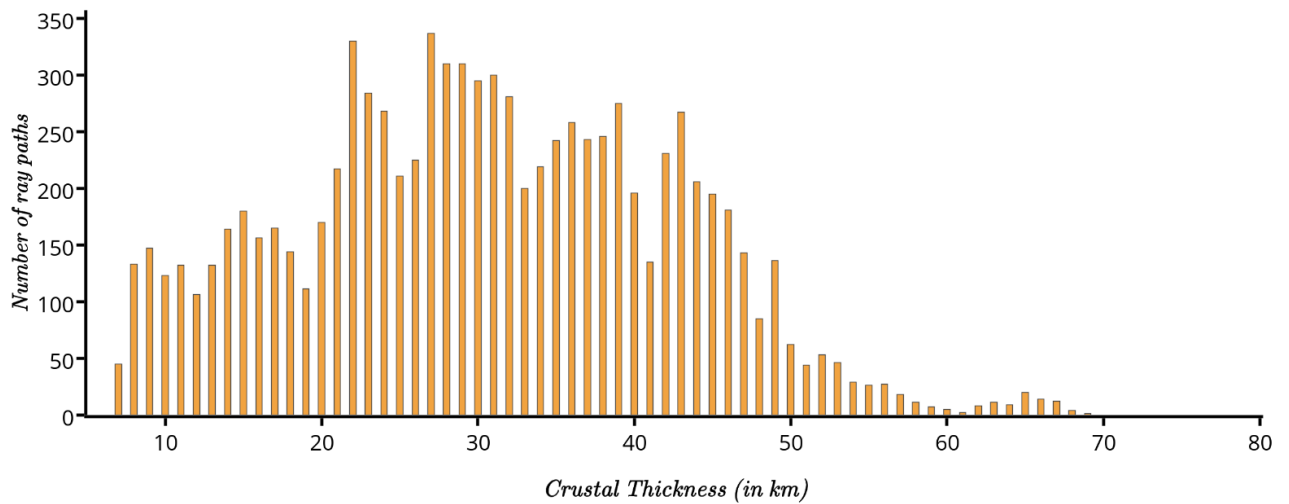


Figure S2.3.1: Bar graph between the average crustal thickness computed using crust-1.0 model [Laske *et al.*, 2013] and the number of paths (for 100s period). Large variations in the average crustal thickness between the source-receiver along the great circle path are observed.

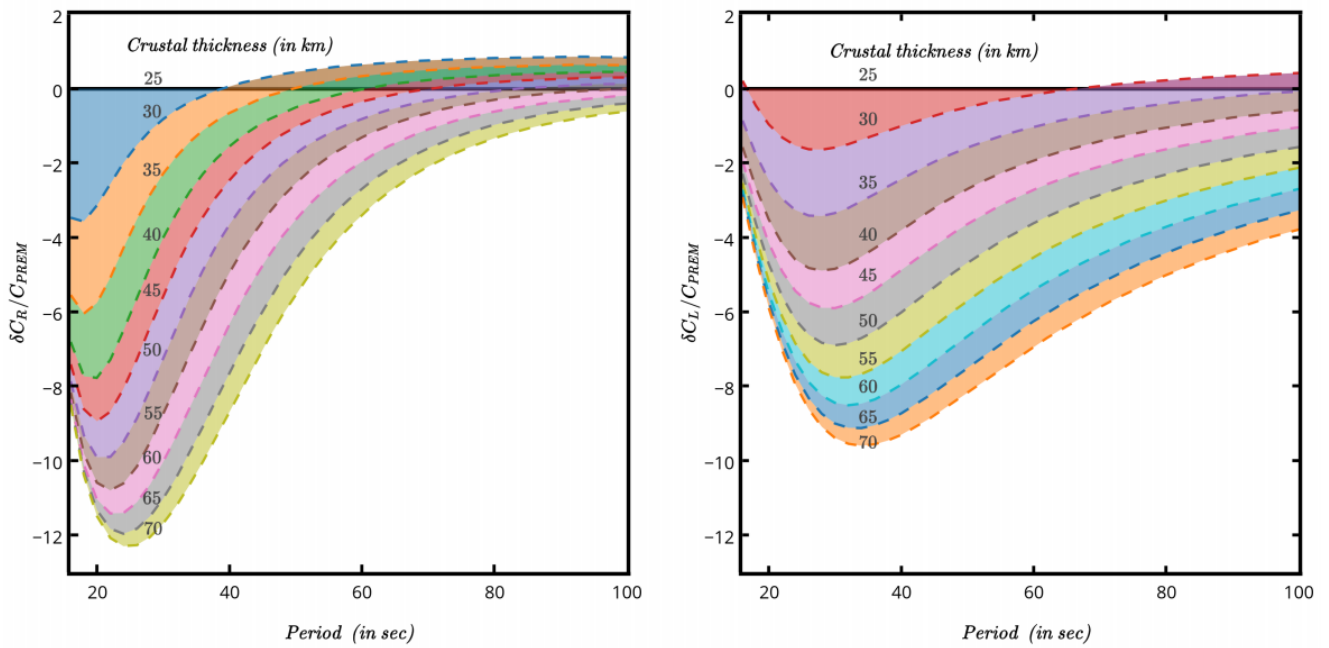
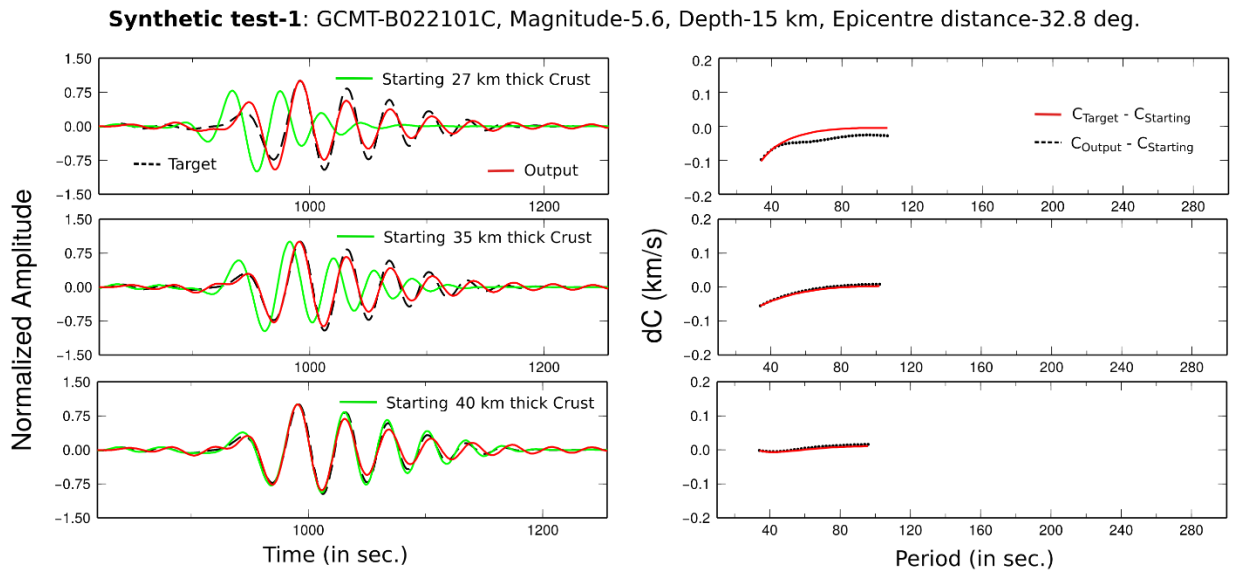


Figure S2.3.2: Synthetic phase velocity perturbation computed using modified crustal thickness of the PREM model with respect to the continental PREM model (dark horizontal line). We observe large variations (2-10 %) in phase velocity anomalies. Rayleigh waves are effected up to 70s and Love waves to even longer periods of 150s.



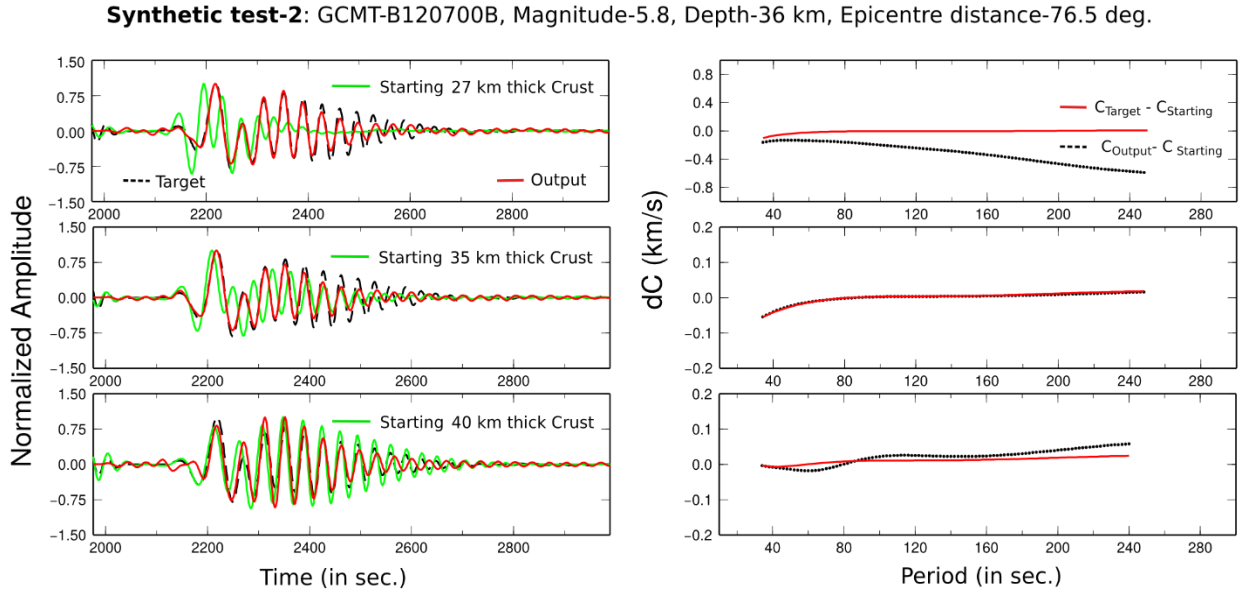


Figure S2.3.3: Effect of different starting models on the synthetic phase velocity dispersion curves used to fit the data. Left panels: Black lines are synthetics computed with a crustal thickness of 35 km and small perturbations in the upper mantle, green lines are synthetics for different crustal thickness values (27,35,40 km) with the PREM model underneath, red lines are the seismograms computed using the models obtained from inversion. Right panels: Corresponding phase velocity difference between observed (red) and recovered (black) dispersion curves from the starting model.

We take into account the influence of crustal thickness by testing various values. For regional and teleseismic events we assume that the average crustal model has more lateral variations due to the crustal thickness (10-75 km) than variations in composition (both velocity and density) between the source-receiver. The average crustal thickness distribution between each source and receiver pair computed using the CRUST-1.0 [Laske et al., 2013] model is shown in figure S2.3.1. Figure S2.3.2 presents large variations in phase velocities due to different crustal thickness values, that can lead to wrong results. Along each path, we used the average crustal model combined with the PREM model (below the crust), as the reference starting model. We present two different test cases in figure S2.3.3 to explain the inversion of phase velocity curves. In both the cases, the average crustal models recover the data. We notice that uncertainties are larger for the long period phase velocity dispersion data due to the inappropriate nature of the starting model.

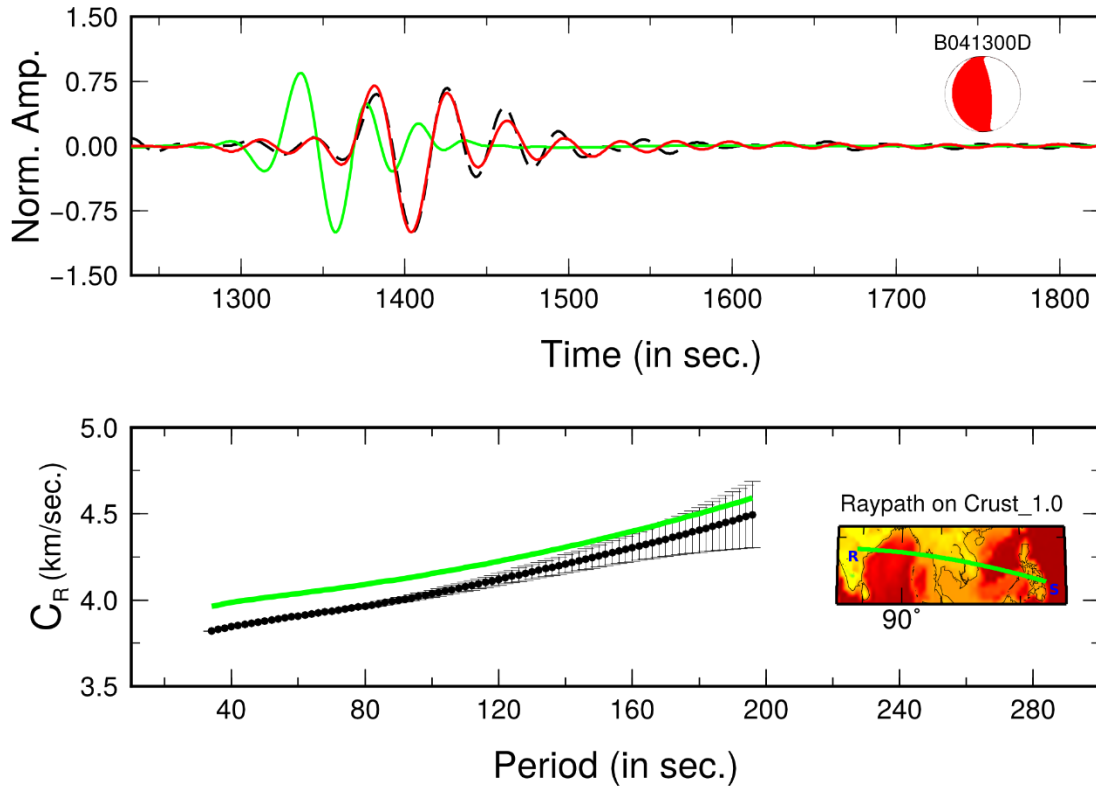


Figure S2.3.4: Top panel : Observed (black dashed line), synthetic (green line) and phase shifted synthetic seismogram computed using the model obtained from inversion using eq. 1. Bottom panel : Starting phase velocity curve (green) and observed phase velocity (black) curve with error bars. Raypath shown in right bottom map, event (S) recorded at HYB (R) seismic station of the GEOSCOPE network.

S3. Regionalization of the dispersion data

S3.1. Selection of the correlation length for Regionalization:

The construction of a covariance function depends on two parameters; a priori uncertainty σ_p at each point and a correlation length L_{corr} . We used 5% for the isotropic term and 1% for the anisotropic term as a priori errors on the parameters, which control the amplitude of the anomaly. The covariance function works in 2D, controlling the number of the independent parameters n_p , where n_p is proportional to the inverse of the square of the L_{corr} [Montagner and Jobert, 1988]. The crust and upper most mantle (first 100 km, dominated by the tectonic features), is more heterogeneous compared to the deeper structure and complexity in the structure decreases in the lithosphere with increasing depth.

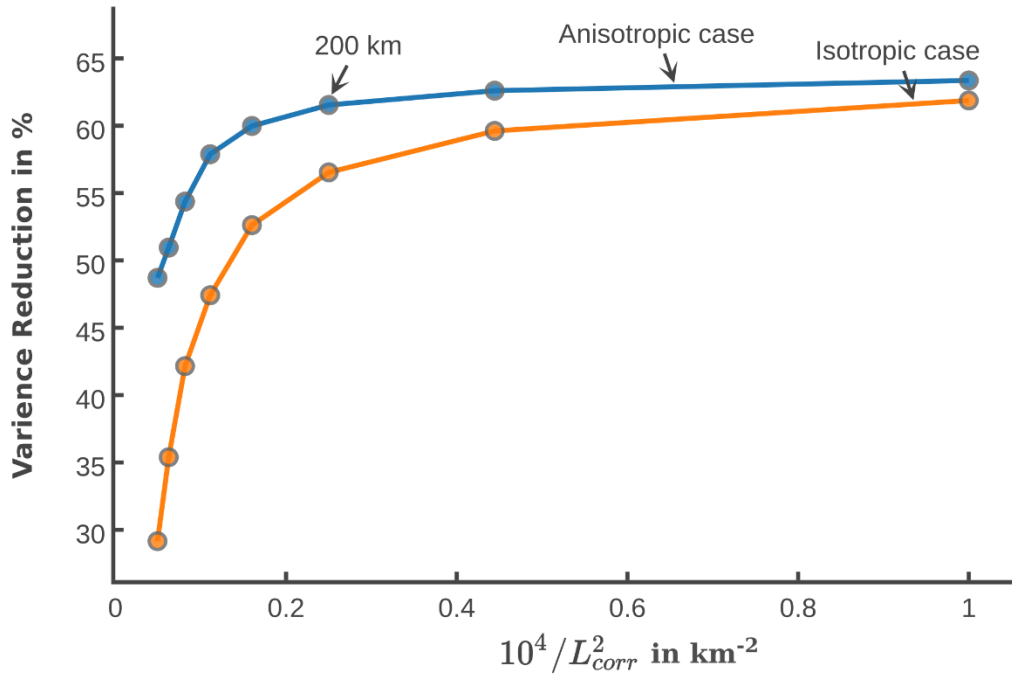


Figure S3.1: Trade-off curves between correlation length and variance reduction at 100s Rayleigh wave phase velocity map.

To better explain the lithospheric structure, we need more number of parameters (n_p) which can observe the sub-lithospheric discontinuity, topography of the discontinuities, anisotropy and heterogeneity etc. To decide the suitable correlation length for our dispersion data, we analyzed the variance reduction in the data for different correlation lengths (figure S3.1). We select a correlation length of 200 km for group and phase to perform the regionalization.

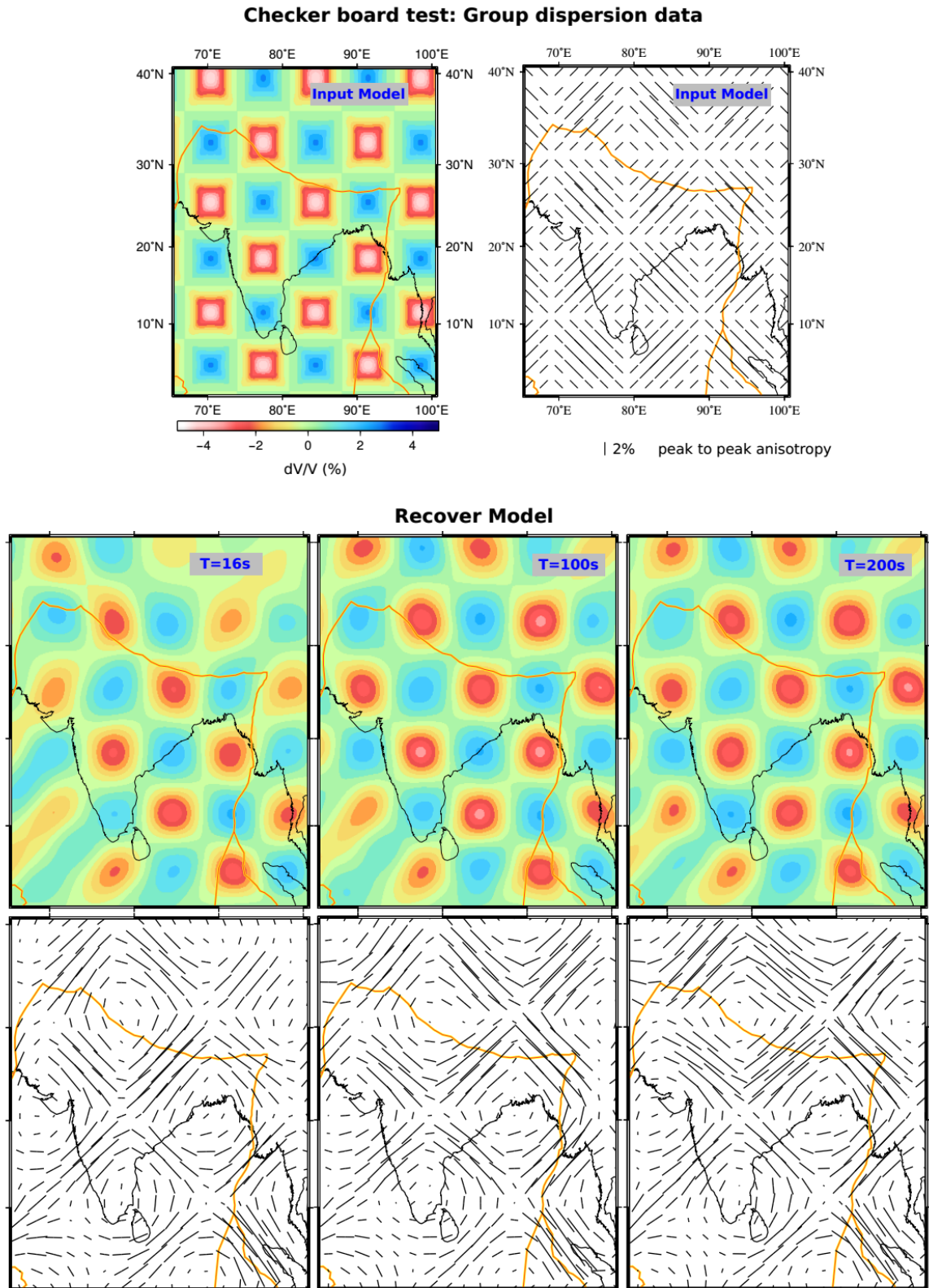
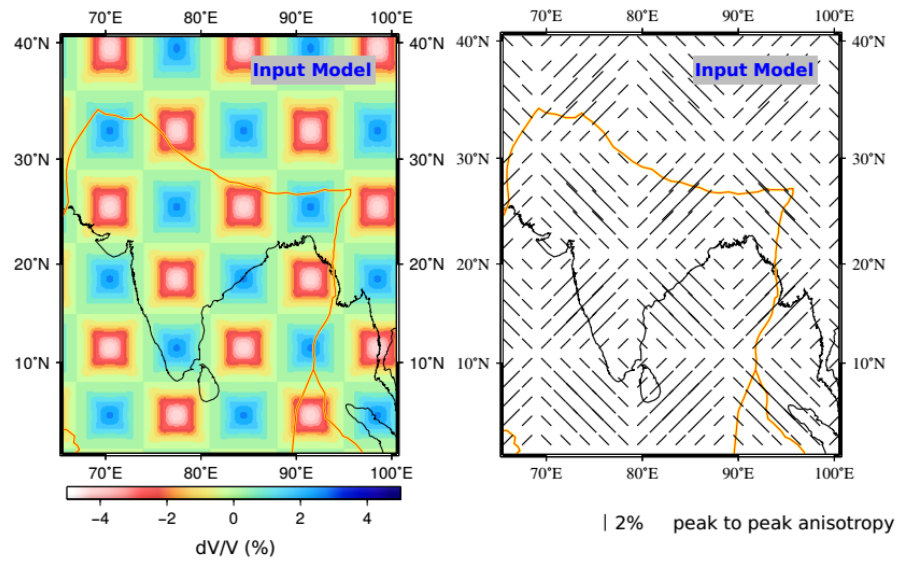


Figure S3.2: Checker board test for the group dispersion data at 16, 100 and 200s with same model parameterization used for real datasets.

Checker board test: Phase dispersion data



Recover Model

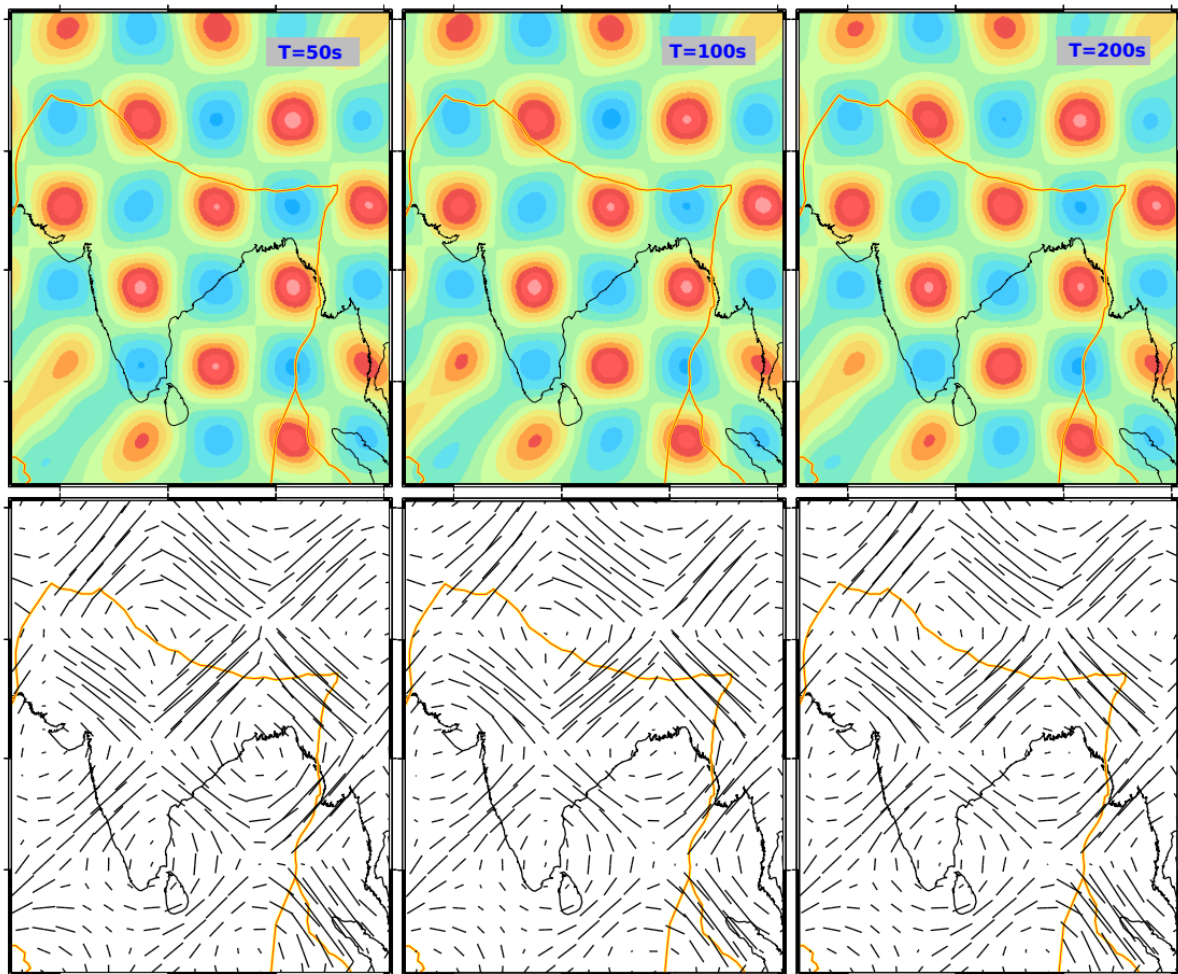


Figure S3.3: Checker board test for the group dispersion data at 50, 100 and 200s, with the same model parameterization used for real datasets.

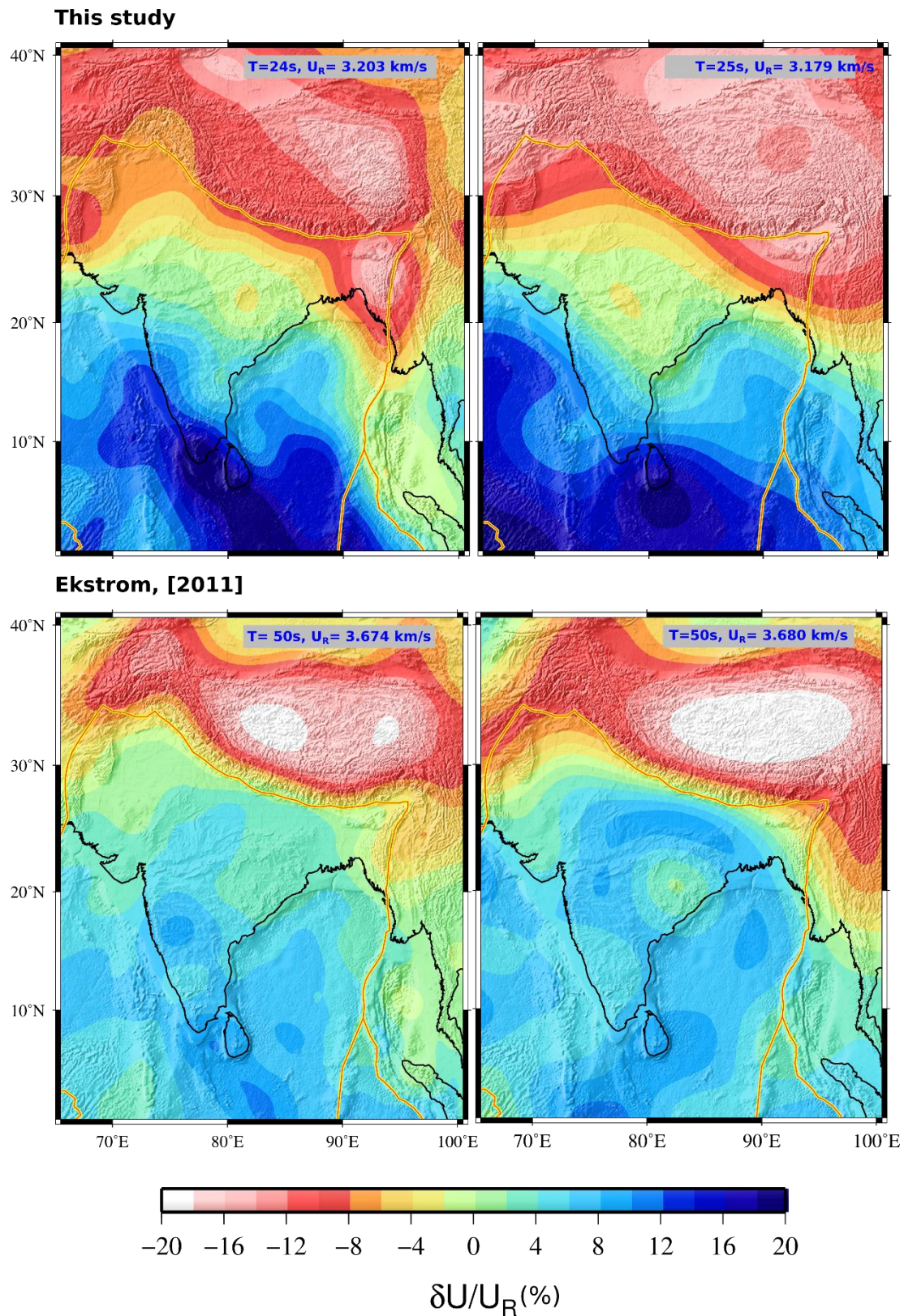
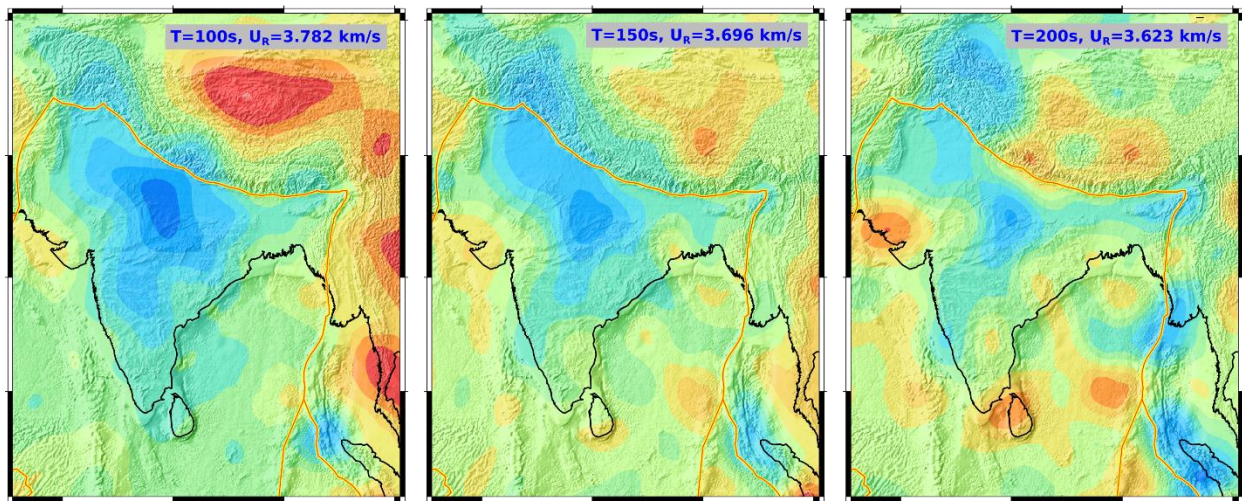


Figure S3.4: Comparison between our group velocity maps and global surface wave short period dataset *Ekström*, [2011]. The perturbations are estimated with respect to the average velocity of the study area.

This Study



Ekstrom, [2011]

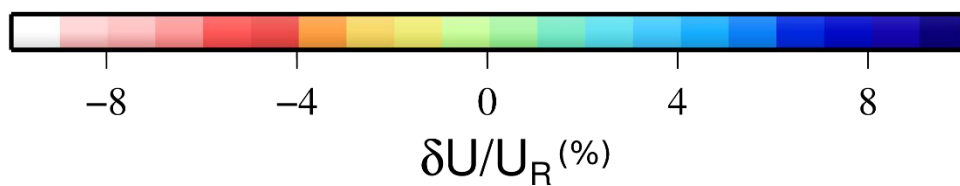
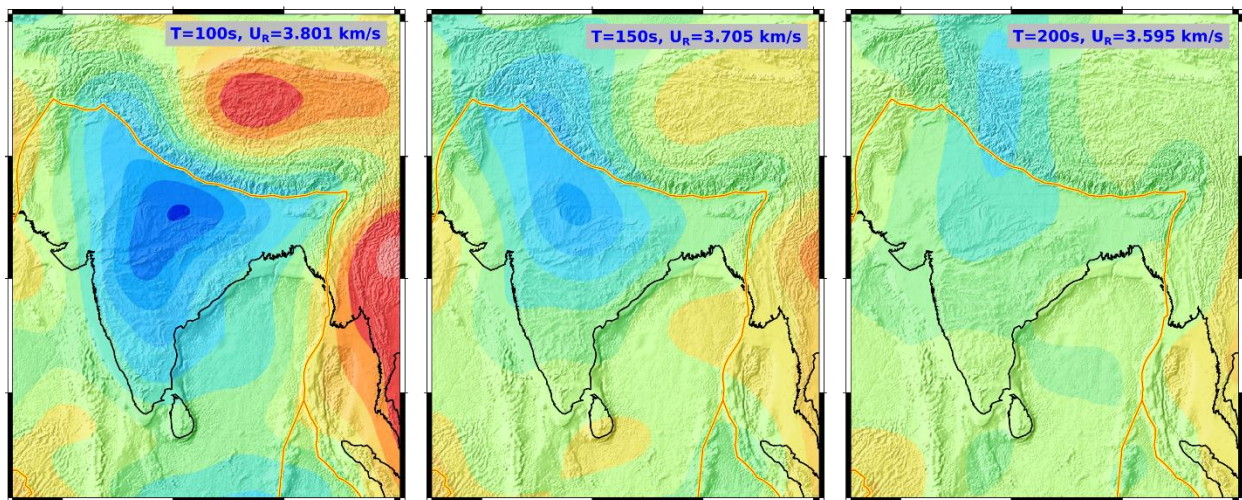
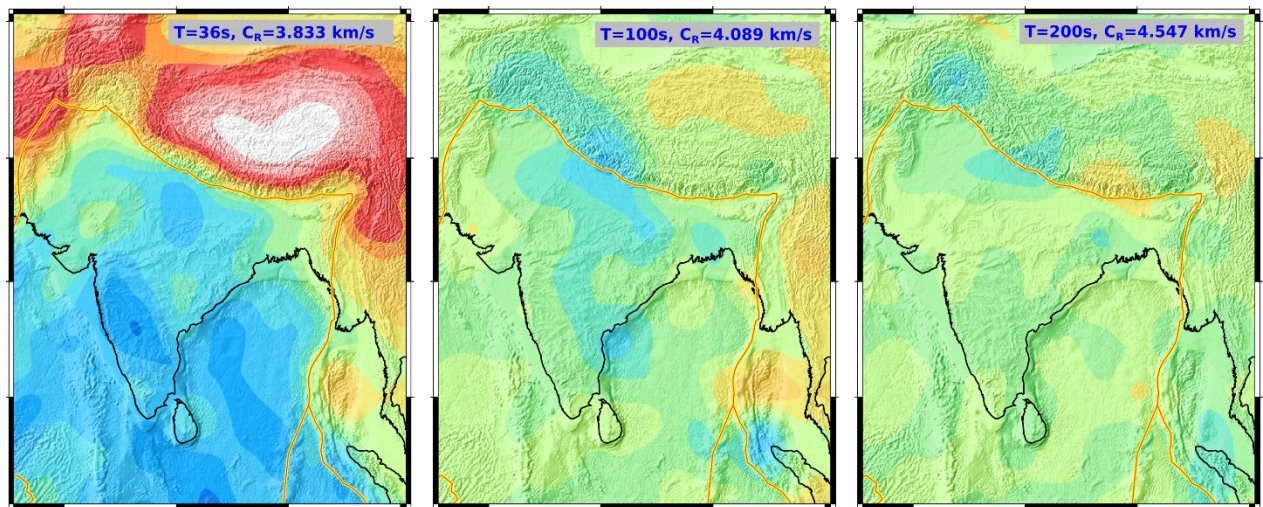


Figure S3.5: Comparison of regionalized group velocity maps at 100s, 150s and 200s from this study and the global surface wave dataset [Ekström, 2011]. The perturbations are estimated with respect to the average velocity of the study area.

This Study



Ekstrom, [2011]

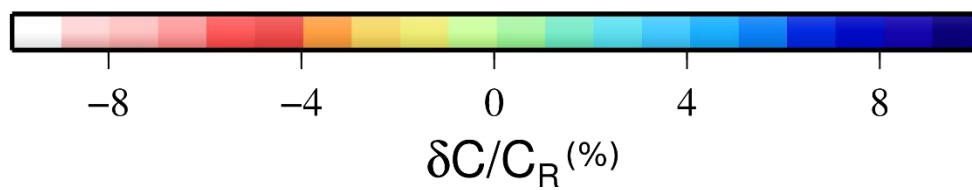
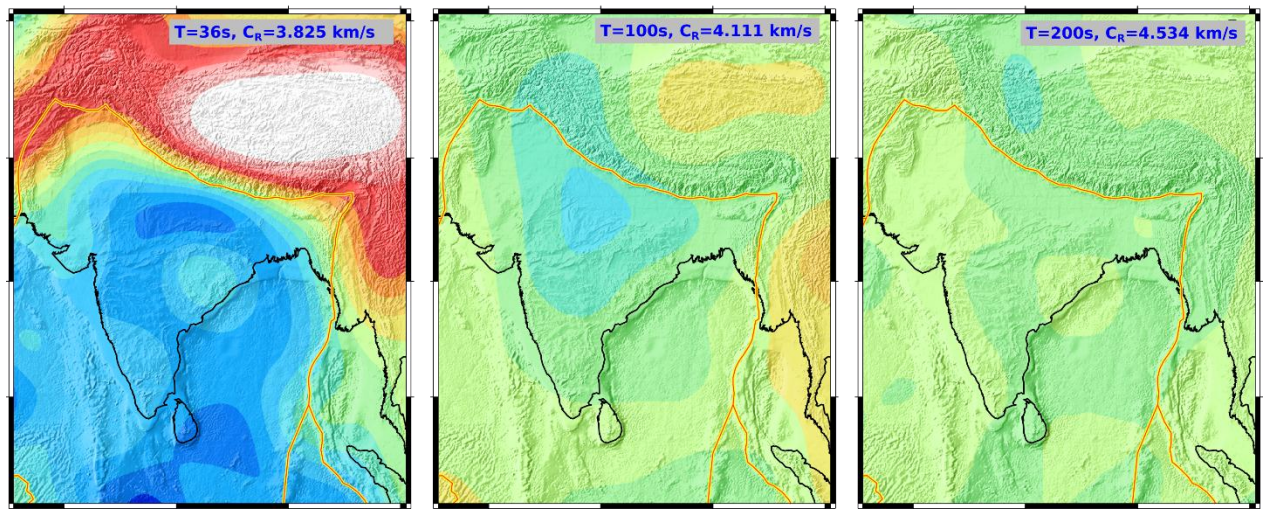


Figure S3.6: Comparison of regionalized phase velocity maps at 36s, 100s and from this study and the global surface wave dataset [Ekström, 2011]. The perturbations are estimated with respect to the average velocity of the study area.

S4: Inversion at Depth

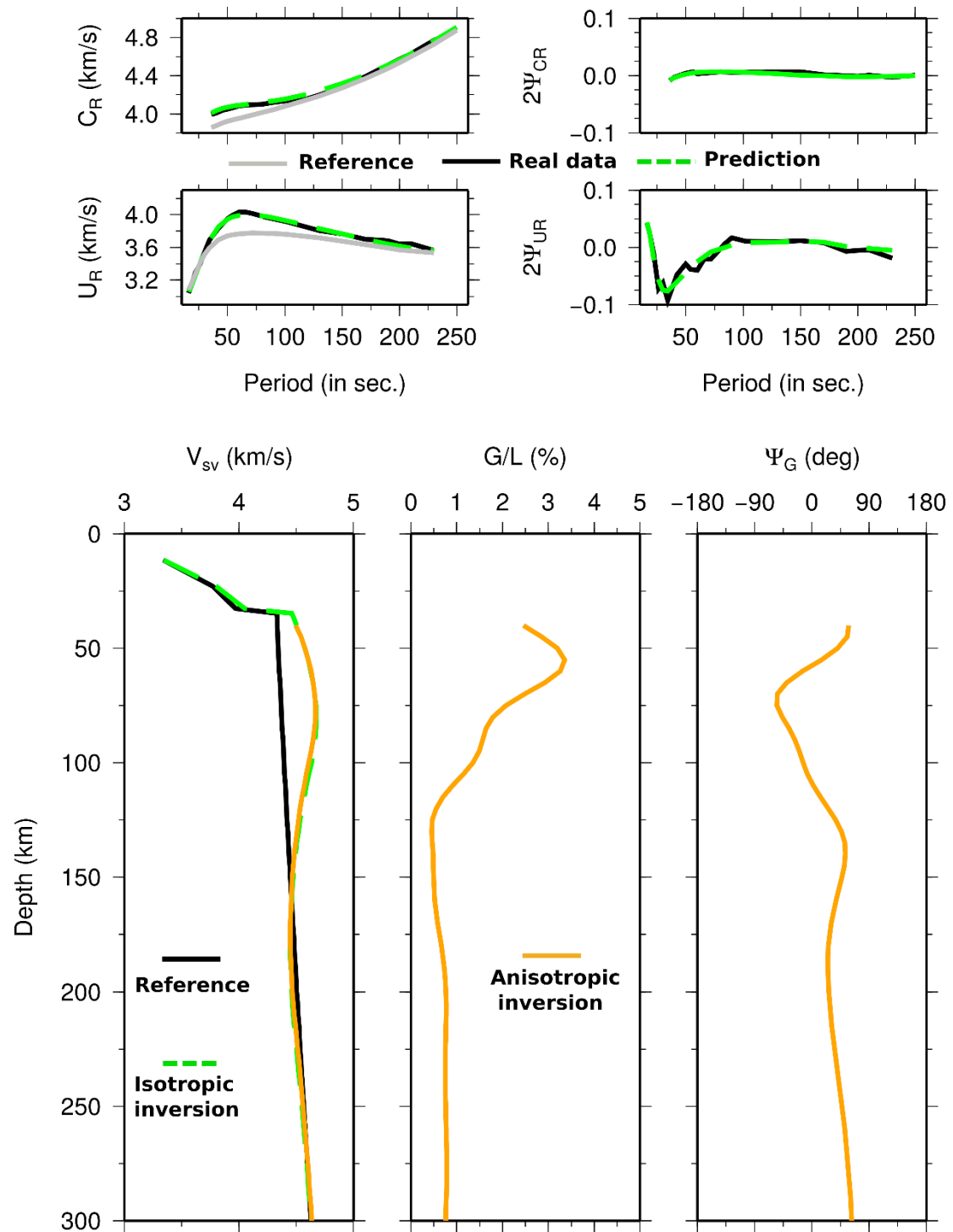


Figure S4: Example showing the depth inversion at a geographical location (17.5,77.5) and comparison with the isotropic/anisotropic model. Anisotropic shear velocity model (in orange) slightly differs from the isotropic shear wave velocity model (in green).

S4.1: Data predictions

To better understand the goodness of the final V_{sv} model in terms of predicting the observed dispersion data, we compute the variance reduction (V.R) using expression:

$$V.R(T) = \left(1 - \frac{\sum_i (V_i^{obs.} - V_i^{Pred.})^2}{\sum_i (V_i^{obs.} - V_i^{Ref.})^2} \right) \quad (S4)$$

Where, at a given period, V is the group or phase velocity at a geographical location i . The regionalized observed and predicted dispersion derived from V_{sv} model are shown in figure S4.2.

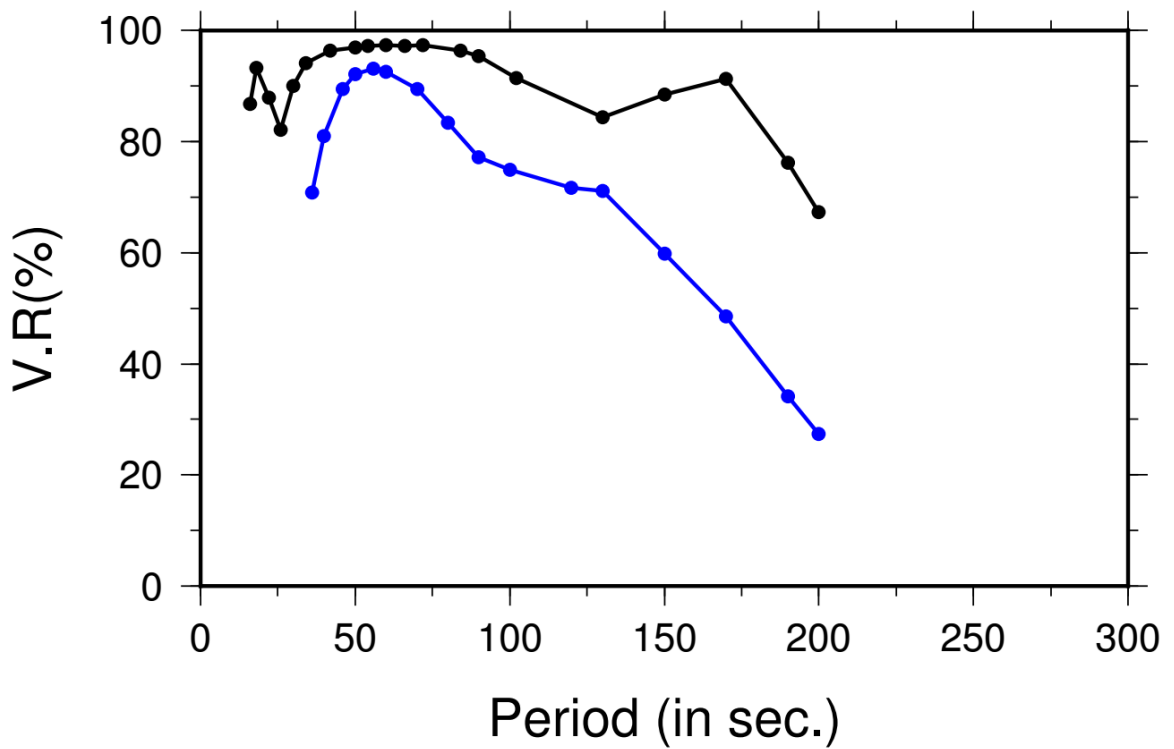


Figure S4.1: Variance reduction plot for group (black) and phase (blue) velocity dispersion. Large variance reduction in short period group velocity data shows significant improvement over the starting crustal and upper most mantle model.

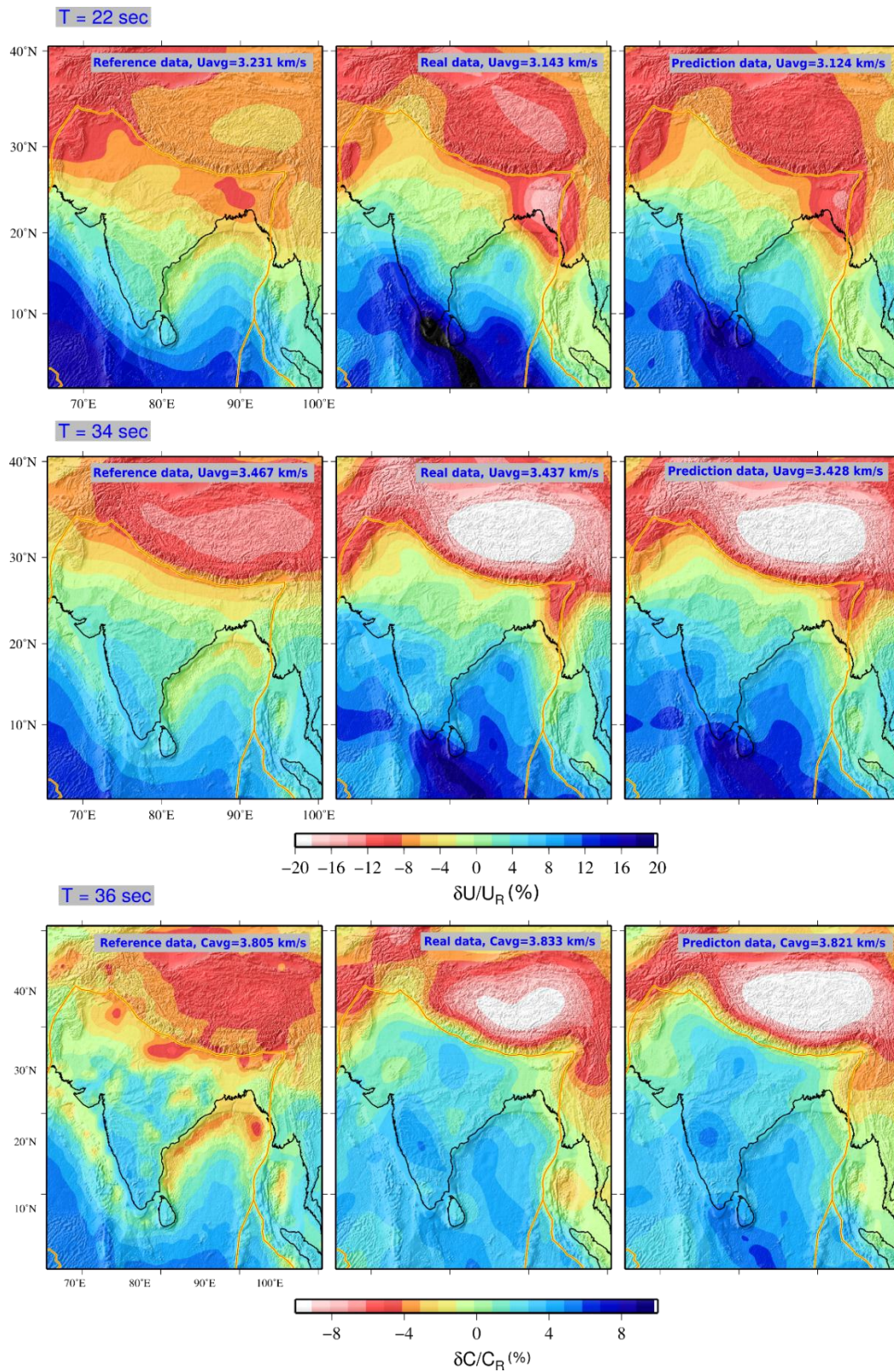


Figure S4.2: Comparison between starting (left), real (middle) and predicted (right) dispersion maps (for group at 22s and 34s, and for phase at 36s) using the shear velocity model obtained in this study. Our predicted model is not affected by the starting model.

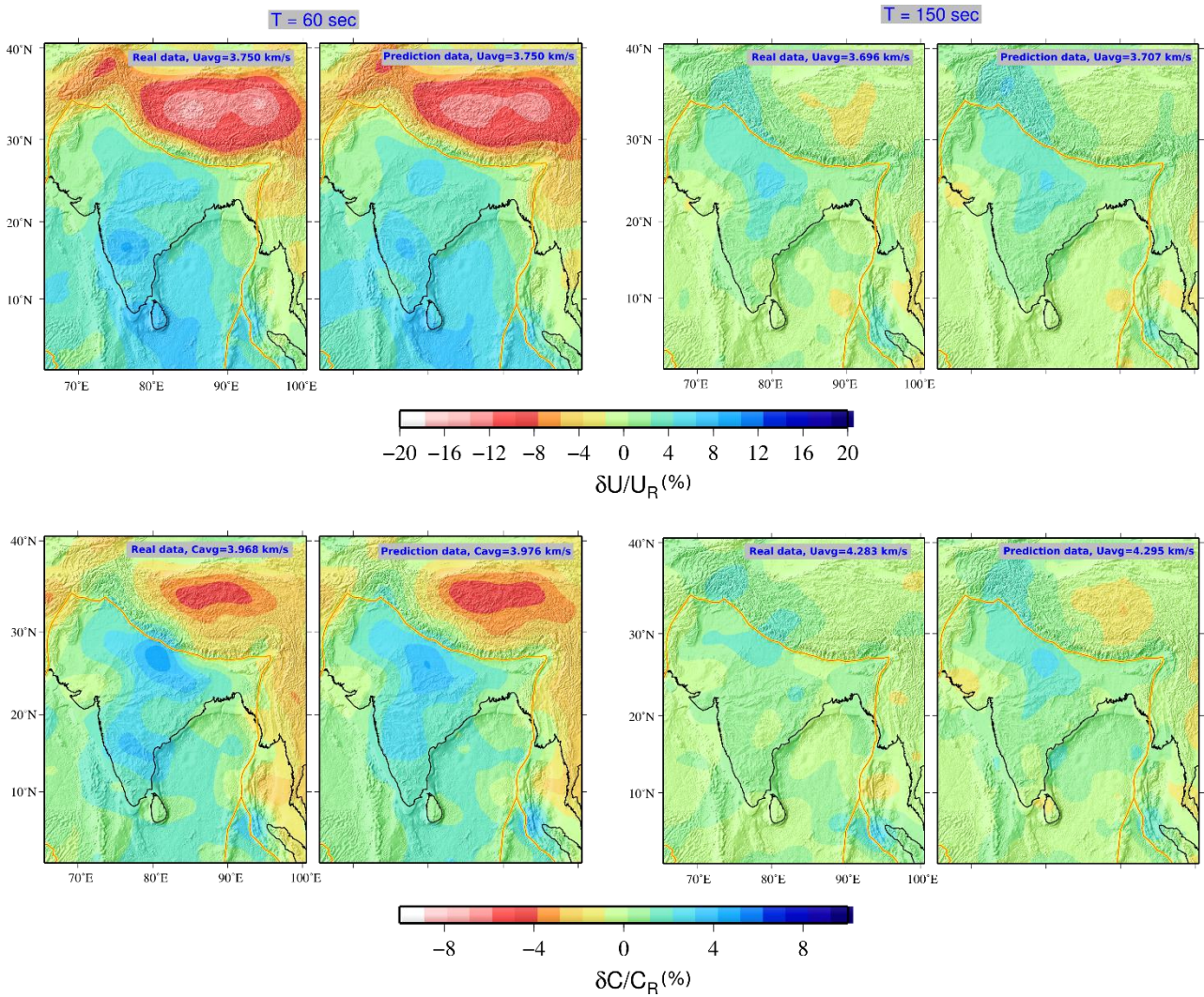


Figure S4.3. Comparison of group (top) and phase (bottom) velocity dispersion maps at 60 and 150s with the predictions from shear velocity models obtained in this study. Good recovery of the phase velocity data with the predicted data is seen at long periods, showing small uncertainty around $\pm 2\%$.

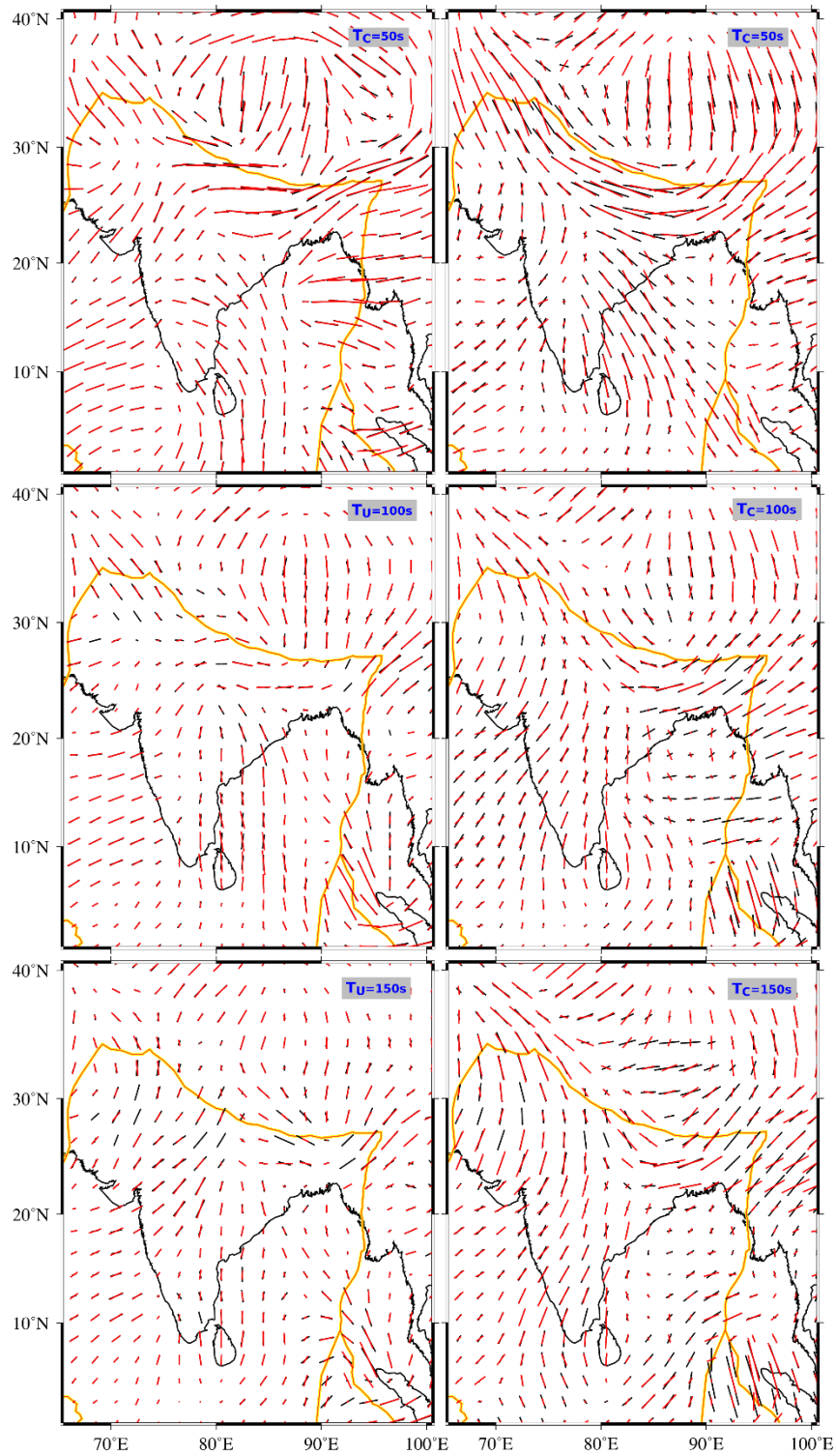


Figure S4.4. Comparison between the fast axis anisotropy directions in black and model predictions in red from anisotropic inversion of group (in left) and phase (in right) velocity dispersion at 50s, 100s and 150s, obtained in this study.

S5: Depth profiles

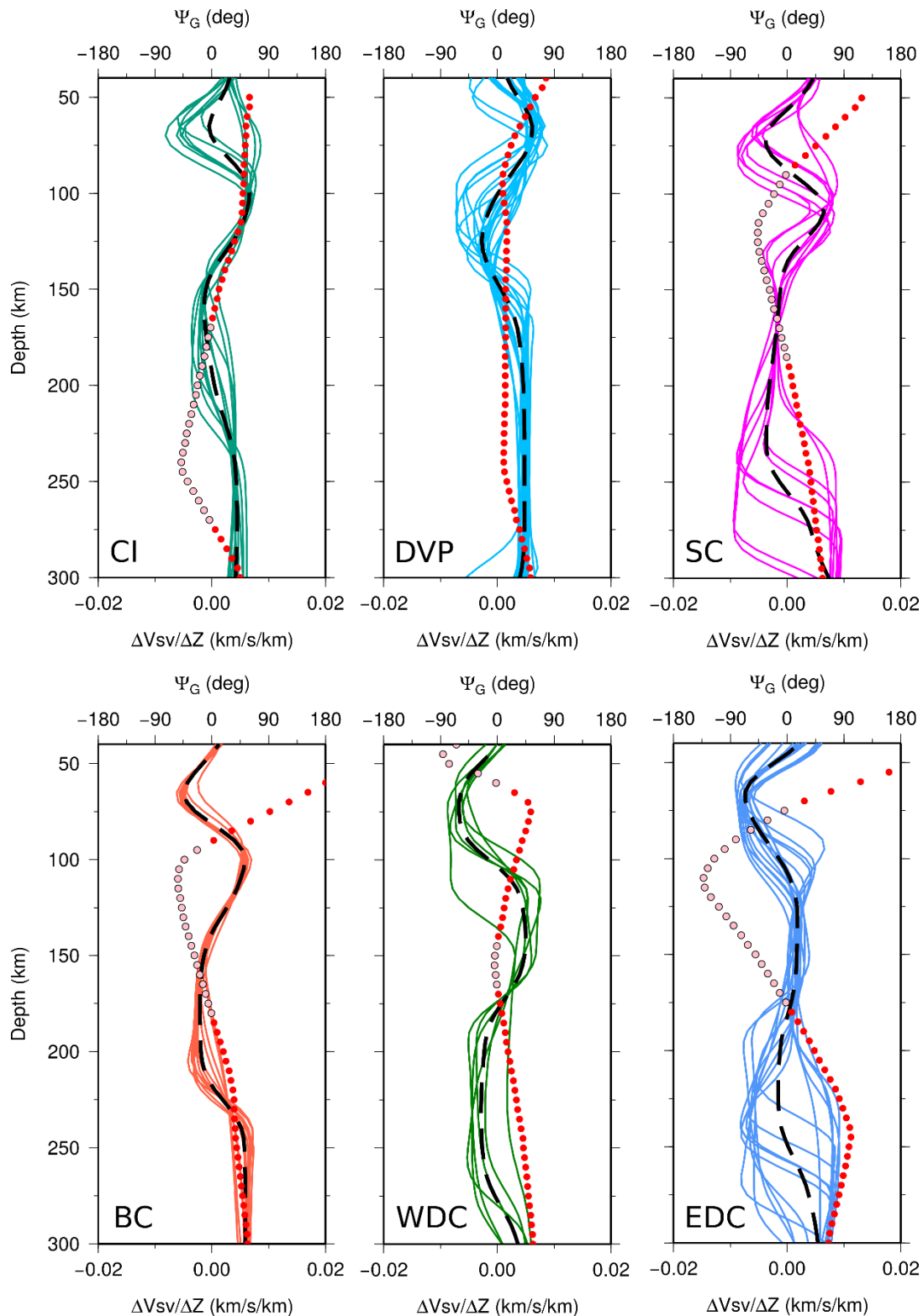


Figure S5.1: Fast axis of azimuthal anisotropy directions for selected profiles (points located in figure S5.2) in the cratonic block. The average curves are shown in solid black. Black dotted lines show the corresponding average velocity gradient and negative values are highlighted as pink dots.

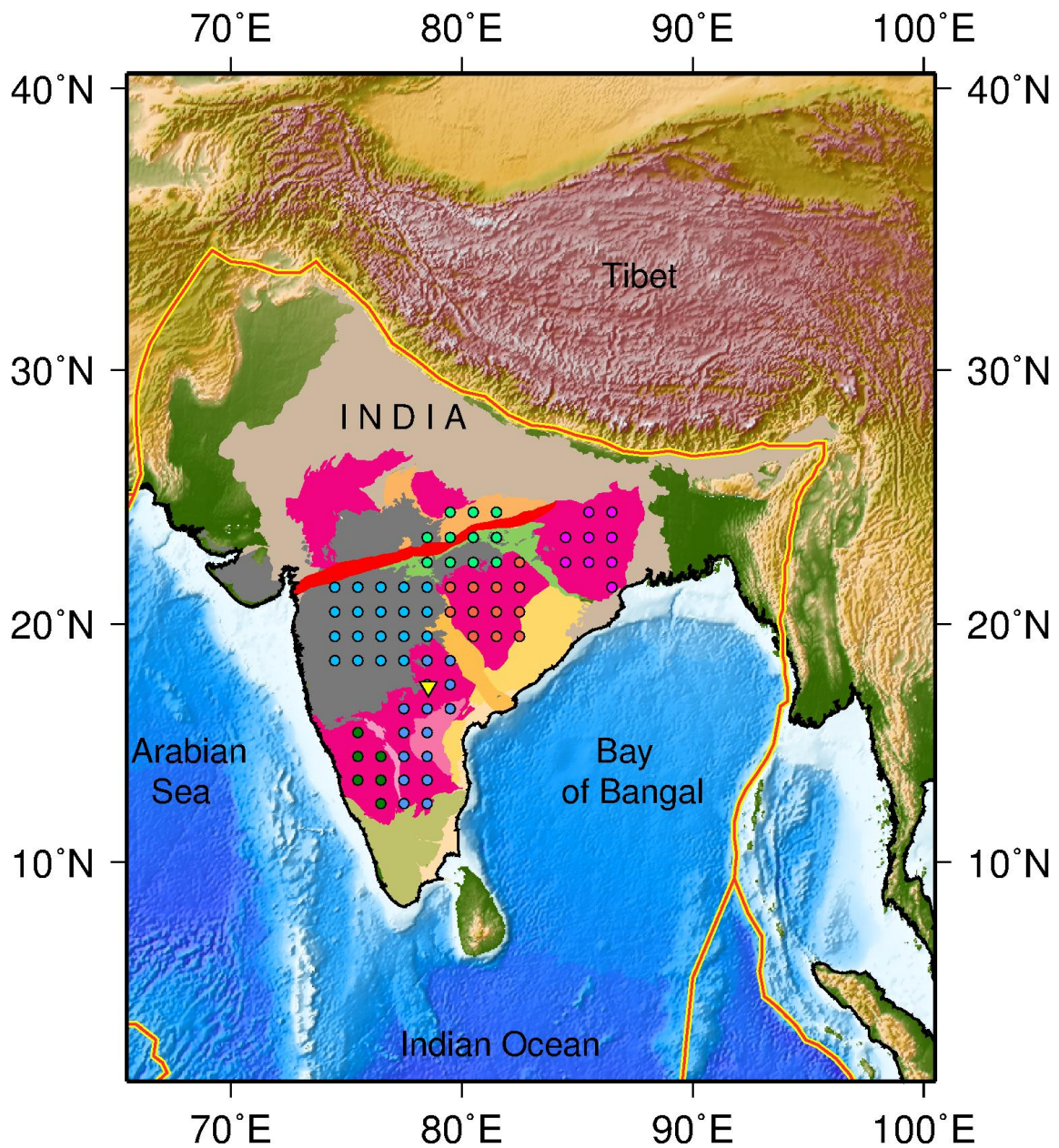


Figure S5.2: Geographical location of the points in the cratonic block selected for presenting the fast axis anisotropy direction and average velocity perturbation profiles in figure S5.1. inverted yellow triangle is the location of HYB seismic station from the GEOSCOPE network.

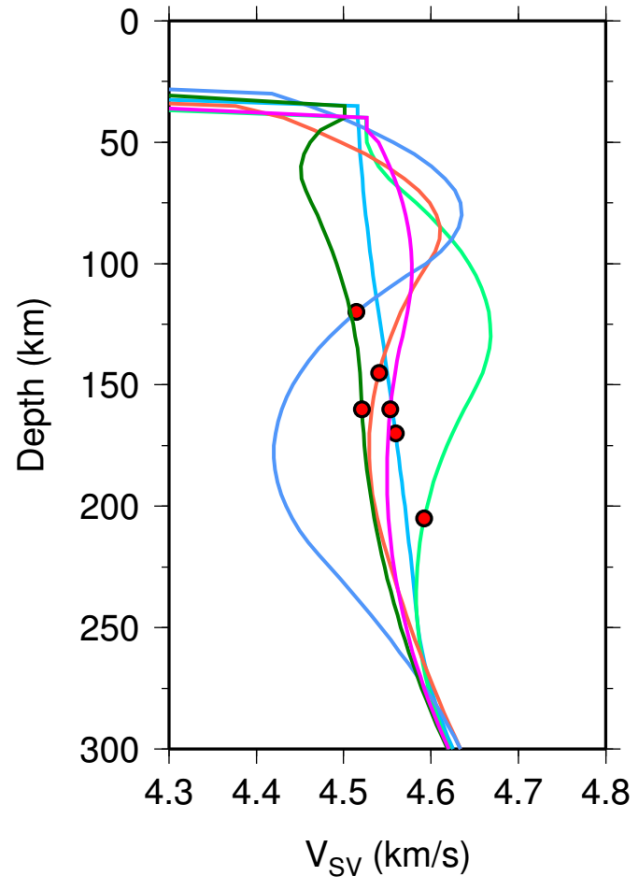


Figure S5.3: Average shear velocity model for six different cratonic blocks whose locations are shown in figure S5.2 with respective colors. Red dots denote respective LAB depths defined by perturbation cut-off ($P_o > 1.25\%$).

S6: Comparison with other shear velocity models

To compare our model with the global models, we measure the Pearson's correlation between four recent global models, as a function of depth using the expression:

$$r = \frac{\sum_l (m_l - \bar{m})(M_l - \bar{M})}{\sqrt{\sum_l (m_l - \bar{m})^2} \sqrt{\sum_l (M_l - \bar{M})^2}} \quad (\text{S6})$$

Where, l is the geographical location, m and M are the shear wave velocities of the two models, and \bar{m} and \bar{M} are the respective means in the study area.

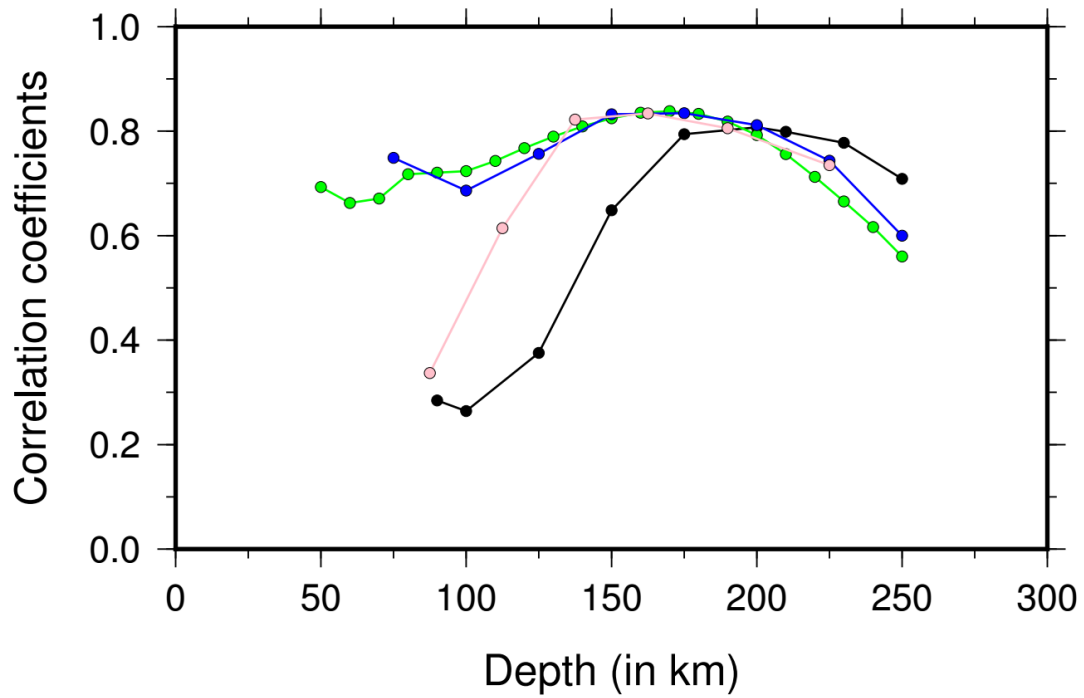


Figure S6.1: Correlation coefficient between our model and four recent global models: *Debayle et al.*, 2016 (black), *Auer et al.*, 2014 (light pink), *French et al.*, 2013 (green) and *Schaeffer and Lebedev*, 2013 (blue), as a function of depth.

Figure S6.1 shows the correlation between all the four models with our model. A good correlation coefficient of 0.75 for deeper depth (>150km), which explains the long period data, shows consistency between our model and these models.

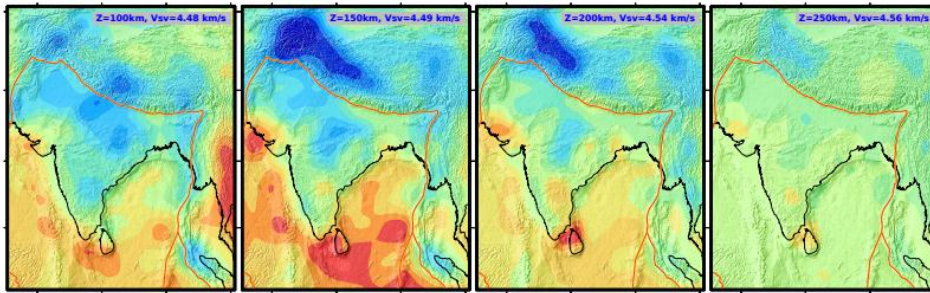
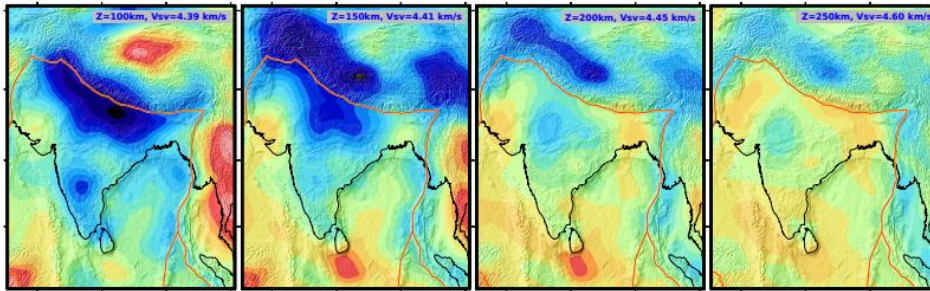
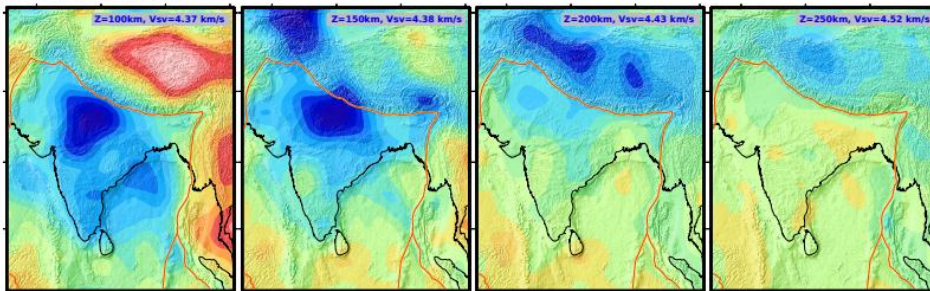
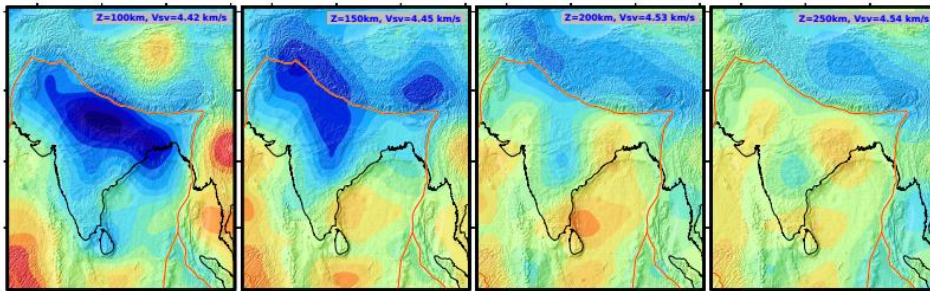
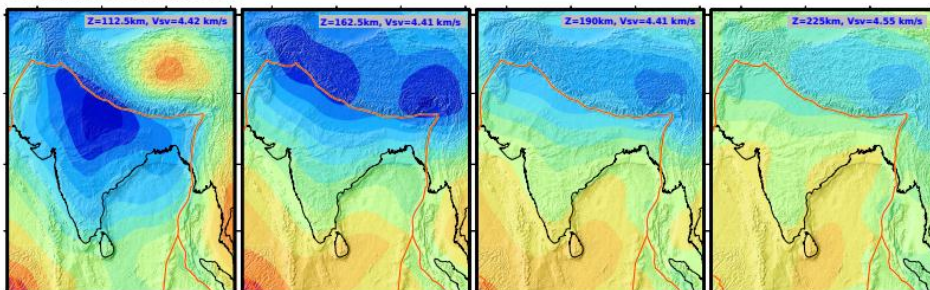
This study**SL2013sv (Schaeffer and Lebedev, 2013)****Debayle et al., 2016****SEMum2 (French et al., 2013)****Savani (Auer et al., 2014)**

Figure S6.2: Comparison of shear velocity perturbation with our and the four recent global models, at depths of 100, 150, 200 and 250km. The perturbations ($\pm 10\%$) are estimated with respect to each average velocity model of the study area.

The decrease in the correlation coefficient at shallow depths maybe due to poor data coverage of data in the study area, used to derive the global models. Bad correlation coefficient at 100 km between our model with *Auer et al.* [2014] and *Debayle et al.*, [2016] model, which can be also seen in Figure S6.2 have strong slow velocity in Tibetan plateau.

References:

1. Auer, L., L. Boschi, T. W. Becker, T. Nissen-Meyer, and D. Giardini (2014), Savani : A variable resolution whole-mantle model of anisotropic shear velocity variations based on multiple data sets, *J. Geophys. Res. Solid Earth*, *119*(4), 3006–3034, doi:10.1002/2013JB010773.
2. Debayle, E., F. Dubuffet, and S. Durand (2016), An automatically updated S -wave model of the upper mantle and the depth extent of azimuthal anisotropy, *Geophys. Res. Lett.*, *43*(2), 674–682, doi:10.1002/2015GL067329.
3. Dziewonski, A. M., and D. L. Anderson (1981), Preliminary reference Earth model, *Phys. Earth Planet. Inter.*, *25*(4), 297–356, doi:10.1016/0031-9201(81)90046-7.
4. Ekström, G. (2011), A global model of Love and Rayleigh surface wave dispersion and anisotropy, 25-250 s, *Geophys. J. Int.*, *187*(3), 1668–1686, doi:10.1111/j.1365-246X.2011.05225.x.
5. French, S., V. Lekic, and B. Romanowicz (2013), Waveform tomography reveals channeled flow at the base of the oceanic asthenosphere., *Science*, *342*(6155), 227–30, doi:10.1126/science.1241514.
6. Laske, G., G. Masters, Z. Ma, and M. Pasyanos (2013), Update on CRUST1.0 - A 1-degree Global Model of Earth's Crust, in *EGU General Assembly Conference Abstracts*, vol. 15, p. 2658.
7. Montagner, J.-P., and N. Jobert (1988), Vectorial tomography--II. Application to the Indian Ocean, *Geophys. J. Int.*, *94*(2), 309–344, doi:10.1111/j.1365-246X.1988.tb05904.x.
8. Schaeffer, A. J., and S. Lebedev (2013), Global shear speed structure of the upper mantle and transition zone, *Geophys. J. Int.*, *194*(1), 417–449, doi:10.1093/gji/ggt095.
9. Tarantola, A., B. Valette, and T. Backus (1982), Generalized nonlinear inverse problems solved using the least squares criterion, *Rev. Geophys.*, *20*(2), 219–232, doi:10.1029/RG020i002p00219.
10. Woodhouse, J. H., and T. P. Girnius (1982), Surface waves and free oscillations in a regionalized earth model, *Geophys. J. Int.*, *68*(3), 653–673, doi:10.1111/j.1365-246X.1982.tb04921.x.